

# **retanalysis-vascx: an explainable software toolbox for the extraction of retinal vascular biomarkers**

Jose D. Vargas Quiros<sup>1,2</sup>, Michael J. Beyeler<sup>5,6</sup>, Sofia Ortin Vela<sup>5,6</sup>, Sven Bergmann<sup>5,6,7</sup>,  
Caroline C.W. Klaver<sup>1,2,3,4</sup> and Bart Liefers<sup>1,2</sup> on behalf of the VascX Research Consortium

<sup>1</sup>Department of Ophthalmology, Erasmus University Medical Center, Rotterdam, the Netherlands

<sup>2</sup>Department of Epidemiology, Erasmus University Medical Center, Rotterdam, the Netherlands

<sup>3</sup>Department of Ophthalmology, Radboud University Medical Center, Nijmegen, the Netherlands

<sup>4</sup>Institute of Molecular and Clinical Ophthalmology, University of Basel, Switzerland

<sup>5</sup>Dept. of Computational Biology, University of Lausanne, Lausanne, Switzerland

<sup>6</sup>Swiss Institute of Bioinformatics, Lausanne, Switzerland

<sup>7</sup>Dept. of Integrative Biomedical Sciences, University of Cape Town, Cape Town, South Africa

# ABSTRACT

**Purpose:** Automatic extraction of retinal vascular biomarkers from color fundus images (CFI) is crucial for large-scale studies of the retinal vasculature. We present VascX, an open-source Python toolbox that extracts biomarkers from CFI artery-vein segmentations.

**Methods:** VascX starts from vessel segmentation masks, extracts their skeletons, builds undirected and directed vessel graphs, and resolves vessel segments into longer vessels. A comprehensive set of biomarkers is derived, including vascular density, central retinal equivalents (CREs), and tortuosity. Spatially localized biomarkers may be calculated over grids placed relative to the fovea and optic disc.

**Results:** VascX is released via GitHub and PyPI with comprehensive documentation and examples. Our test-retest reproducibility analysis on repeat imaging of the same eye by different devices shows that most VascX biomarkers have moderate to excellent agreement ( $ICC > 0.5$ ), with important differences in the level of robustness of different biomarkers. Our analyses of biomarker sensitivity to image perturbations and heuristic parameter values support these differences and further characterize VascX biomarkers.

**Conclusions:** VascX provides an explainable and easily modifiable feature-extraction toolbox that complements segmentation to produce reliable retinal vascular biomarkers. Our graph-based biomarker computation stages support reproducible, region-aware measurements suited for large-scale clinical and epidemiological research.

**Translational Relevance:** VascX supports oculomics research by enabling easy extraction of existing biomarkers and rapid experimentation with new biomarkers. Its robustness and computational efficiency facilitate scalable deployment in large databases. Open-source distribution via PyPI lowers barriers to adoption for ophthalmic researchers and clinicians.

# Introduction

Artificial intelligence (AI) has rapidly changed ophthalmic research by enabling the quantitative, automated analysis of imaging at scale. Modern deep learning (DL) applied to color fundus imaging (CFI) has demonstrated the ability to automatically detect ophthalmic disease. In recent years, the field of oculosomics has taken this a step further by utilizing the eye to understand systemic health<sup>1-3</sup>. Non-invasive CFI allows for time and cost-efficient examination of the arteriolar and venular retinal vasculature, also opening the door for large-scale analysis of the vasculature in existing population-based cohorts and clinical databases. Today, substantial evidence links key retinal vascular features to hypertension, kidney disease, stroke subtypes, and overall cardiovascular risk<sup>2</sup>.

Relevant retinal vascular biomarkers include the central retinal arteriolar/venular equivalents (CRAE/CRVE), artery-vein ratio (AVR), bifurcation angles, tortuosity/fractal dimension, and bifurcation counts. These features capture changes in the vasculature due to hypertension, hemodynamic status, and network remodeling/efficiency, and have each been linked to target organ damage and incident vascular events<sup>2,4</sup>.

Prior work on the technical challenge of automatically extracting biomarkers from CFIs has laid a strong foundation. Several papers made use of combined vessel segmentations (arteries and veins in a single segmentation map) to extract parameters such as fractal dimension (a measure of complexity), vessel density, vessel diameters, and tortuosity metrics<sup>5,6</sup>. Recently, datasets, models, and feature extraction pipelines have been developed to segment and analyze the artery and vein vessel trees separately<sup>7-11</sup>. PVBM provides a modular Python toolbox for computing a diverse set of vascular biomarkers from pre-segmented vessel maps, including branching angles, endpoints, and intersections<sup>12</sup>. AutoMorph delivers a comprehensive end-to-end DL pipeline that includes standardized morphological measurements like caliber, tortuosity, and measures of vascular complexity<sup>9</sup>. Together, these tools have made vascular analysis on CFIs more accessible to researchers

Nevertheless, important technical gaps remain. Most notably, PVBM and AutoMorph do not use the location of the fovea for feature computation, preventing the extraction of more localized biomarkers computed over regions or grids defined relative to the optic-disc-fovea axis. The topological data representation in both tools is limited to an undirected graph, preventing the extraction of topological features that rely on the directedness of the vessel tree graph. Furthermore, both tools lack utilities for easily visualizing the computed features, which limits interpretability. On the application side, the reproducibility across devices and the robustness of different retinal vascular parameters to imaging conditions

has not been characterized before, making it difficult for researchers to understand the reliability of different parameters, their variants, and the effect of configuration parameters or heuristic choices.

VascX addresses the technical needs with a graph-based feature extraction toolbox that utilizes AI disc segmentations and fovea locations for localized feature extraction<sup>10</sup>. The pipeline transforms image-level vessel masks into four different representations sequentially: skeletons, undirected graphs, directed trees with the optic disc as the root, and resolved vessel trees. Biomarkers are then computed from the most appropriate representation stage (e.g., mask-based density, node-based bifurcation counts/angles, segment-based diameter/length/tortuosity, and OD–fovea–aligned spatial features such as CRE and temporal arcade angles). Critically, VascX computes local features using grids and regions defined relative to the fovea and optic disc landmarks, facilitating harmonized reporting and region-specific analyses relevant to clinical translation.

In this paper, we present and characterize a transparent, well-documented, and easily modifiable Python toolbox designed to accelerate methodological innovation and large-scale, reproducible oculomics research. Our contributions are the following:

- We provide an easy-to-use toolbox for analyzing the retinal vasculature. Our toolbox can compute a comprehensive catalog of morphology, topology, caliber, and spatially localized biomarkers, including OD–fovea–aligned and ETDRS-style grid features, from artery–vein–resolved segmentations. VascX enables rapid experimentation with improved retinal biomarkers via a clear, modular graph-based pipeline and well-documented APIs. We provide a comprehensive characterization of VascX biomarker reproducibility and sensitivity. We present results on the test-retest reproducibility of VascX biomarkers across images of the same eye, but captured using different devices. We complement these results with a sensitivity analysis using artificial perturbations of input images to test the sensitivity of VascX against image quality degradation. Finally, we characterize how optional parameters of VascX that define computation regions and thresholds affect biomarker outputs.
- The VascX toolbox is open source and easily accessible in Python via PyPI as `retinalysis-vascx`

## Methods

Our package was developed entirely in Python using standard data science and image manipulation packages: numpy, opencv, Pillow, scikit-learn, skimage. The package has only open-source dependencies. In this work, we present a first public version of the package. We will follow semantic versioning for future versions.

The VascX feature extraction pipeline operates on image segmentations (usually generated by AI models) and outputs a CSV file with features or biomarkers computed from them. The previous step of model segmentation has been addressed in previous work<sup>8-10</sup>. VascX operates on image files individually or in bulk. It accepts all input image formats readable by Pillow.

## Software Summary

VascX is available at:

<https://github.com/Eyened/retinalysis-vascx>

under an open-source license (GNU Affero General Public License v3.0). The package is also available in the Python package index (PyPI) under the name `retinalysis-vascx`.

## Usage

Installation of the VascX feature extraction pipeline amounts to creating a virtual environment and installing the pipeline as a Python package:

```
pip install retinalysis-vascx
```

We provide helpers and instructions for running in batches. The entire pipeline can be run in two stages:

**1. Segmentation.** To extract all the necessary segmentations from the images:

```
vascx run-models <INPUT_DIR> <SEGMENTATIONS_DIR>
```

This command will store model output segmentations and some intermediate files in a folder structure with matching filenames:

```
<SEGMENTATIONS_DIR>  
- preprocessed_rgb - preprocessed fundus images  
- artery_vein - artery-vein model segmentations  
- vessels - vessel model segmentations
```

- disc - optic disc model segmentations
- bounds.csv - contains the bounds of the fundus image
- fovea.csv - model predictions of the fovea locations for each image
- quality.csv - model estimations of CFI quality

This command makes use of previously published segmentation, regression, and keypoint localization AI models<sup>10</sup> to segment vessels, arteries, veins, and disc, obtain fovea locations, and estimate image quality. Note that this step requires a GPU with at least 8GB VRAM. The folders (preprocessed\_rgb, artery\_vein, vessels, disc) contain matching filenames (one per input image). The CSV files contain one row per input image.

**2. Biomarker extraction.** The second stage operates on the output from the first stage:

```
vascx calc-biomarkers <SEGMENTATIONS_DIR> <OUTPUT_CSV_FILE> --feature_set full_v3 --n-jobs 8 --logfile <LOG_FILE>
```

Where `<SEGMENTATIONS_DIR>` is the path to the directory used in step 1, `<OUTPUT_CSV_FILE>` is the desired output file path, and `<LOG_FILE>` is an optional file path for logging errors and warnings. This step is CPU-only and benefits from parallel execution for performance. The `--n-jobs` option may be changed depending on the number of available CPU cores.

## Vascular biomarker computation

VascX processes the input artery-vein model segmentations into separate artery and vein masks. These are then separately processed through four main stages of computation, each producing different data representations:

- **Input masks:** `np.ndarray[bool]` per layer; optic disc and fovea metadata from segmentation models.
- **Stage 1 - Skeleton:** We first hole-fill the predicted binary vessel map to obtain a clean binary mask; when an optic disc mask is available, the disc region is excluded to prevent spurious centerlines. The skeleton is computed with `skimage` skeletonization on binary, yielding single-pixel-wide centerlines that preserve network topology. This pixel-level representation underpins coverage and diameter sampling and serves as the substrate for graph construction.
- **Stage 2 - Undirected graph:** From the skeleton, we build a NetworkX Graph whose nodes correspond to end/junction points and whose edges follow the chain of centerline pixels between them. Each edge carries a `Segment` that stores the ordered centerline, arclength and geometric summaries; splines are fitted on

demand to the centerline to enable robust diameter and angle estimation. This representation supports segment-level filtering and aggregation without yet imposing flow direction.

- **Stage 3 - Directed digraph:** We orient the undirected graph into a DiGraph by rooting each connected component at the optic disc and directing edges away from the disc. Roots are identified as the end-node per component closest to the disc center. Vessel segments are directed edges carrying geometry and derived properties (length, median diameter, curvature). The directed graph representation is an intermediate step in the identification of bifurcations. A distance-transform-based assignment maps each pixel in the binary vessel mask (stage 1) to its nearest segment.
- **Stage 4 - Resolved vessels:** In previous stages, vessel segments are defined only between nodes in the skeleton/graph representation. This means that the presence of even a small vascular branch on a large vessel will cause it to be split into two segments. To facilitate the computation of biomarkers on longer, potentially more anatomically relevant vessel trajectories, we run a recursive vessel-resolution algorithm on the DiGraph. For each root, an aggregated caliber is propagated along outgoing paths using a length-weighted running statistic of per-edge median diameters. At every bifurcation, the branch with the largest aggregated caliber is taken as the principal continuation; non-selected branches are closed and emitted as resolved segments. Consecutive edges along a resolved path are concatenated into a single Segment by merging centerlines (and attached pixels), yielding a simplified directed graph whose `resolved_segments` approximate individual vessels between major bifurcations. This reduces fragmentation from skeletonization while preserving topology for trajectory-level tortuosity and OD-fovea-aligned measures.

Finally, biomarkers are extracted from one or a combination of these data representations. Mask-based biomarkers, such as vascular density, for example, are calculated on the input masks, while topological features, such as bifurcation angles, use the directed graph and nodes extracted in stage 4. Figure 1 exemplifies the different stages of computation for a sample set of CFIs.

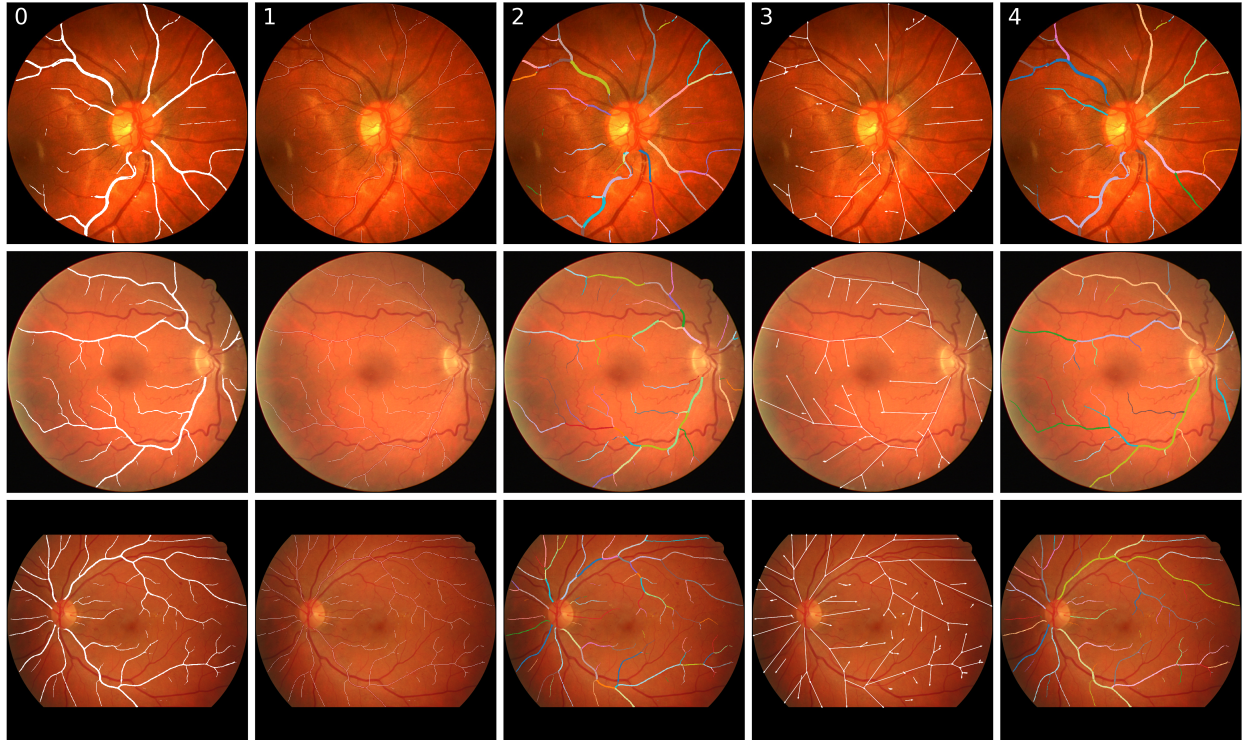


*Figure 1. From left to right, stages of computation in the VascX pipeline for three sample CFIs: 0) input binary mask for the arteries, 1) skeletonization or centerline computation, 2) vessel segments are extracted from the skeleton, and mapped back to their centerline and mask, 3) a directed graph consisting of multiple trees with the optic disc as root, 4) segments are resolved into potentially more anatomically meaningful structures for biomarker measurements.*

## Biomarkers

VascX computes retinal vascular biomarkers from standardized representations (binary masks, undirected/directed graphs, resolved vessels). Below we describe each biomarker with the exact quantity being estimated and the equations used. Throughout,  $B$  denotes the stage-1 binary vessel mask,  $S$  the set of eligible directed segments with lengths ( $l_i$ ), and  $R$  an analysis region of interest; cardinalities count pixels, and distances are in pixels unless noted.

**VascularDensity.** The fraction of retinal area occupied by vessels in  $R$ , computed on the binary mask  $B$ :

$$D = \frac{|B \cap R|}{|R|}.$$

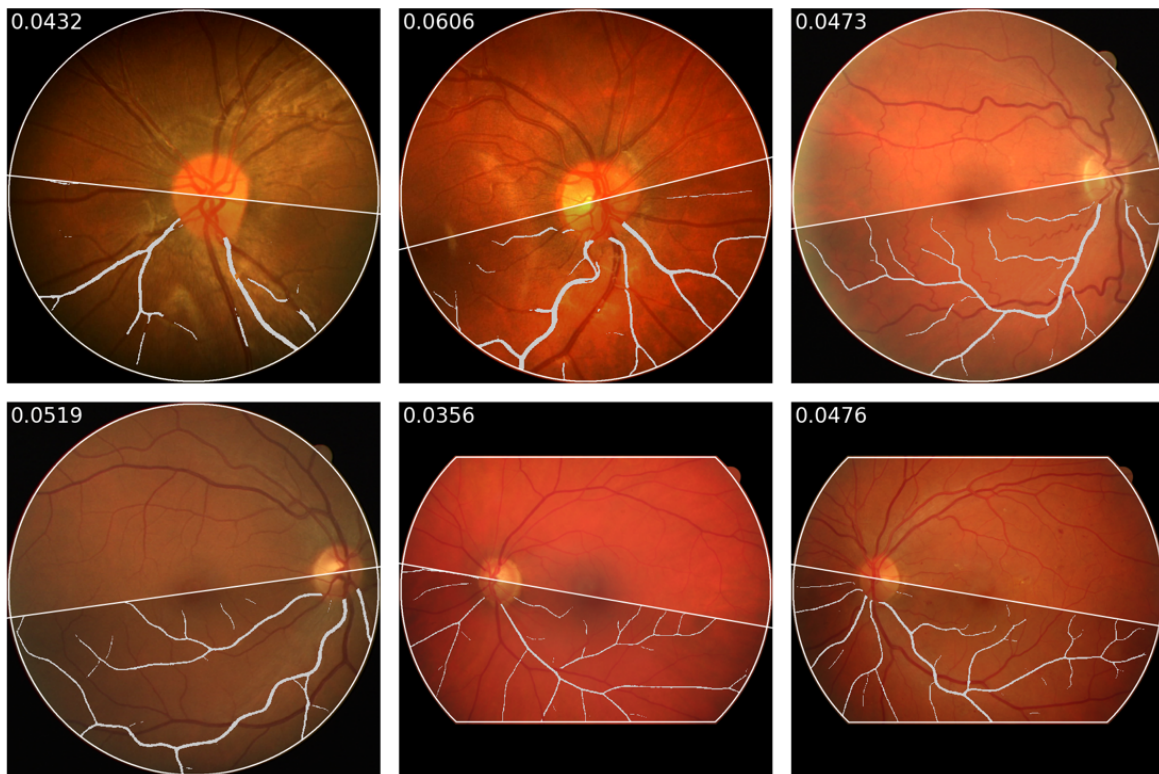


Figure 2. Examples of vascular density computation on the lower hemifield. The computed value is show on the top left corner of each sample.

**BifurcationAngles.** For each bifurcation  $b$  at position  $p_b$ , outgoing branch directions are estimated by sampling the branches' splines at distance  $\delta$  from the node along each branch at points  $q_1$  and  $q_2$ . Unit vectors  $(u_b, v_b)$  are defined from the bifurcation point to the sample points:

$$u_b = \frac{q_1 - p_b}{\|q_1 - p_b\|}, \quad v_b = \frac{q_2 - p_b}{\|q_2 - p_b\|},$$

and the bifurcation angle is defined as the angle between these vectors:

$$\theta_b = \arccos(u_b \cdot v_b), \quad \theta_b \in [0^\circ, 180^\circ].$$

Angles exceeding  $160^\circ$  are discarded as non-bifurcating continuations. Summary statistics (e.g., mean/median) are reported across valid nodes.

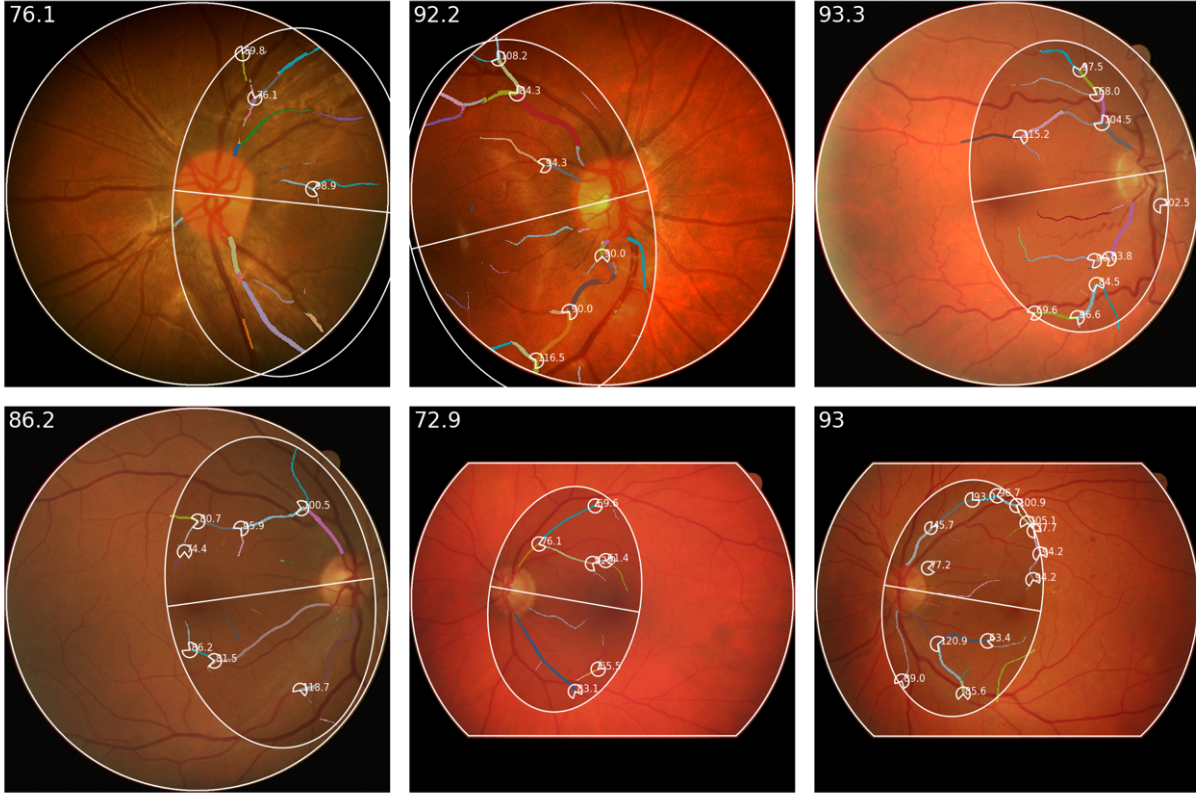


Figure 3. Examples of bifurcation angle computation on an elliptical region located between the fovea and optic disc. This region is consistently visible in optic disc and macula-centered images. The computed value is show on the top left corner of each sample.

**Caliber.** For each segment  $i$ , diameters are sampled along a spline fitted to its skeleton by projecting spline normals to the vessel boundary on B. The per-segment diameter is the median along its arclength. The reported caliber aggregates over eligible segments (length  $\ell_i \geq \ell_{\min}$ ):

$$\text{Caliber} = g(\{d_i: i \in S\}),$$

where  $(g)$  is a robust statistic (typically the median).

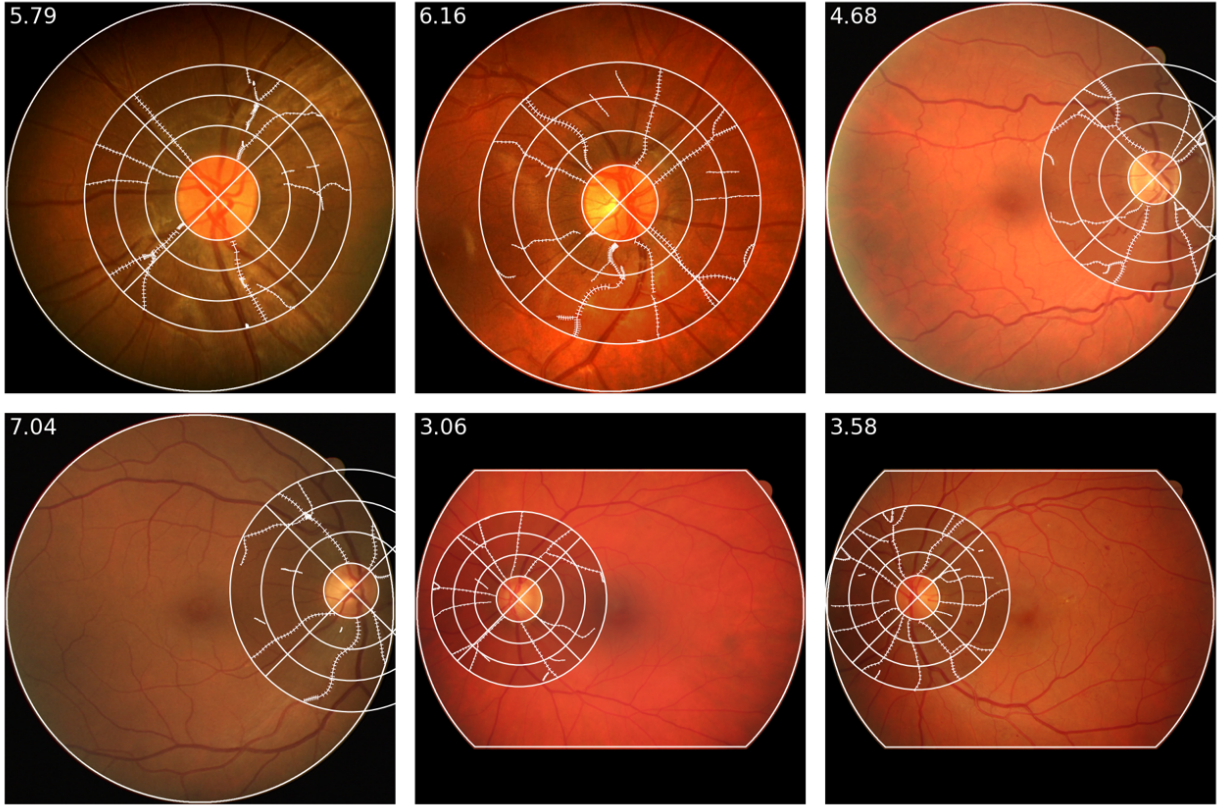


Figure 4. Examples of caliber computation over a region defined around the optic disc. The computed value is show on the top left corner of each sample.

**Tortuosity.** Three complementary measures are provided per segment (or per resolved vessel). Let  $L_{arc,i}$  be arclength and  $L_{chord,i}$  the end-to-end Euclidean distance.

- Distance factor:

$$T_i^{DF} = \frac{L_{arc,i}}{L_{chord,i}}.$$

- Curvature-based measure, using planar curvature  $\kappa_i(s)$  and OD-fovea distance  $d_{ODF}$  for scale normalization:

$$T_i^K = \frac{1}{L_{arc,i}} \int_0^{L_{arc,i}} |\kappa_i(s)| ds \cdot d_{ODF}.$$

- Inflection count (number of curvature sign changes along the centerline):

$$T_i^{INF} = N_{\text{inflections}}^{(i)}.$$

When reporting a single score over multiple segments, length-weighted aggregation may be used for normalization:

$$T_{\text{tot}} = \sum_{i \in \mathcal{S}} \left( \frac{\ell_i}{\sum_{j \in \mathcal{S}} \ell_j} \right) t_i,$$

with  $t_i$  any of the measures above.

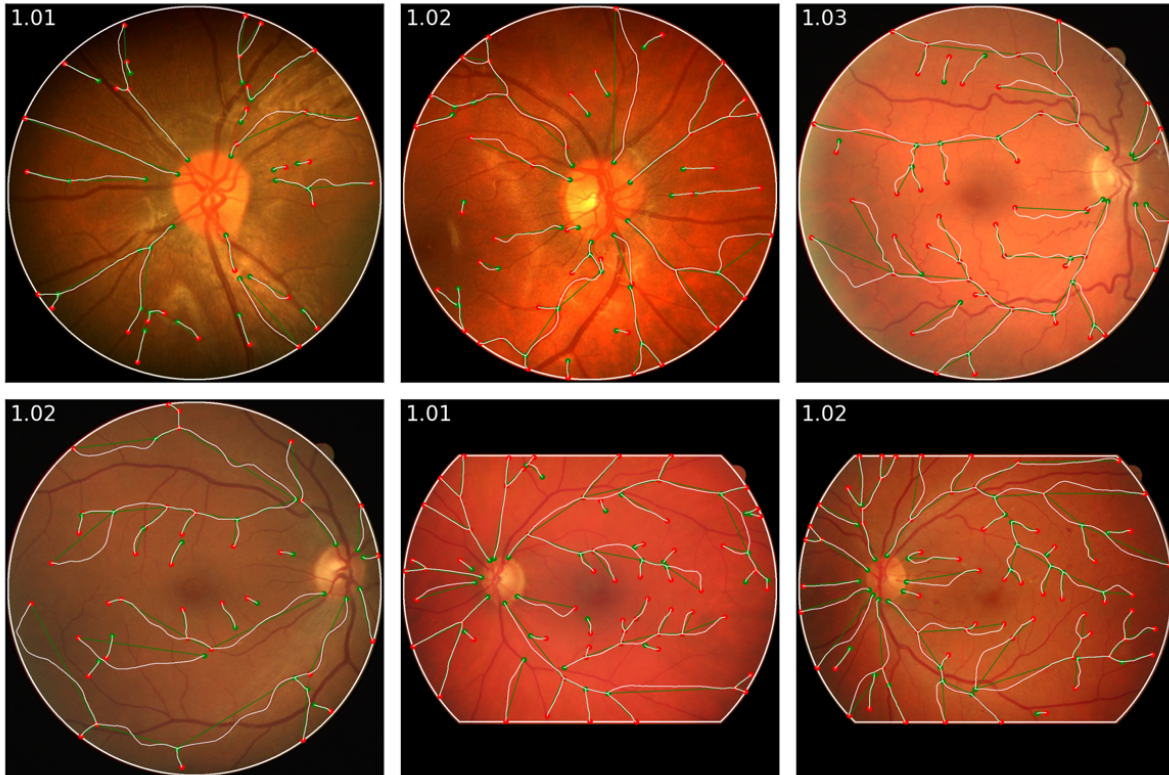


Figure 5. Examples of tortuosity computation over the entire visible region. The computed value is show on the top left corner of each sample.

**CRE (Central Retinal Equivalents).** CREs are calculated using the revised formulas by Knudtson et. al.<sup>13</sup> Concentric circles centered at the optic disc are intersected with the vessel network. At each radius  $r$ , up to  $M$  vessel segments with the largest median diameters are retained. The vessel segments are paired and recursively reduced via the Hubbard rule with a constant  $c$  (arteries: 0.88; veins: 0.95):

$$d \leftarrow c \sqrt{d_1^2 + d_2^2}$$

Where  $d_1$  and  $d_2$  are the diameters of the paired vessels. The formula is applied recursively until a single equivalent caliber  $d_r$  remains. The final CRE is the median of  $\{d_r\}$

across radii. For details about the pairing and reduction procedure please refer to Knudtson et. al. <sup>13</sup>

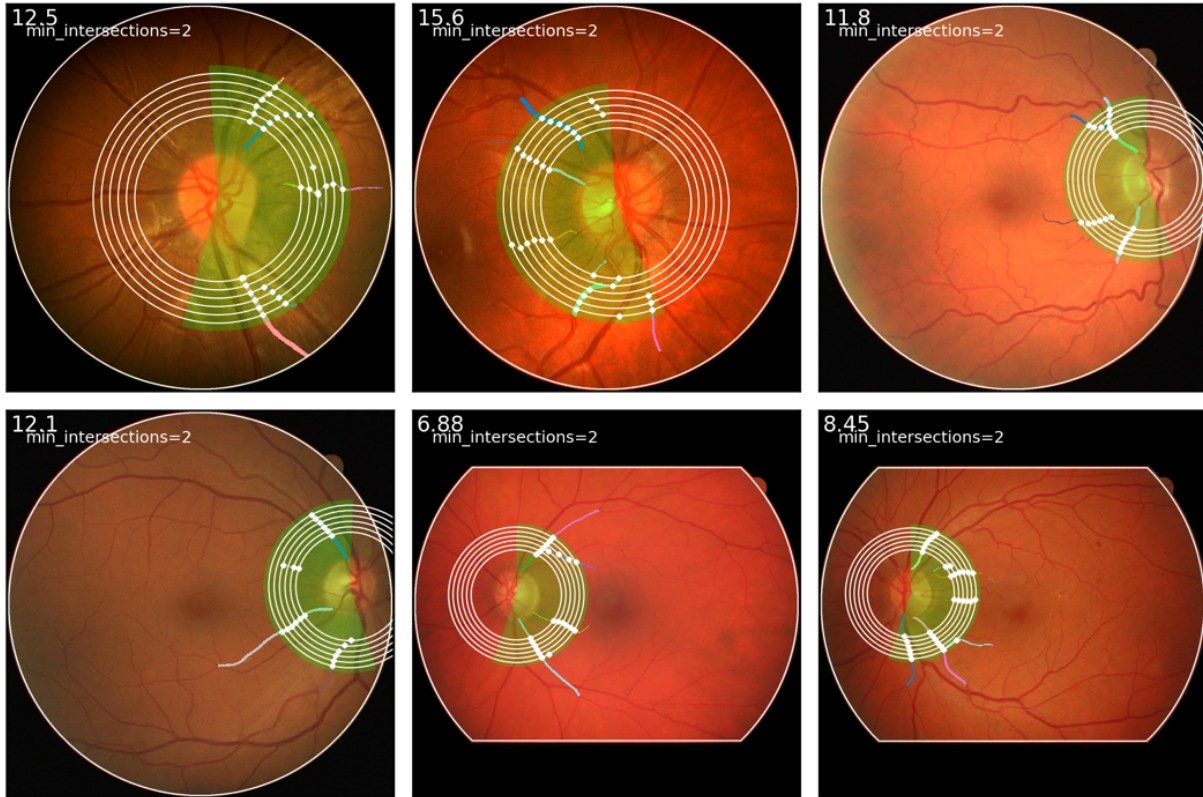


Figure 6. Examples of central retinal equivalent (CRE) computation on the superior hemifield. The computed value is show on the top left corner of each sample.

**TemporalAngle.** On each concentric circle of radius ( $r$ ), the two dominant temporal vessels are identified by diameter and spatial continuity. The angle at the disc center is

$$\theta_r = \angle(\overline{OD p_1(r)}, \overline{OD p_2(r)}),$$

and the reported value is the median over radii.

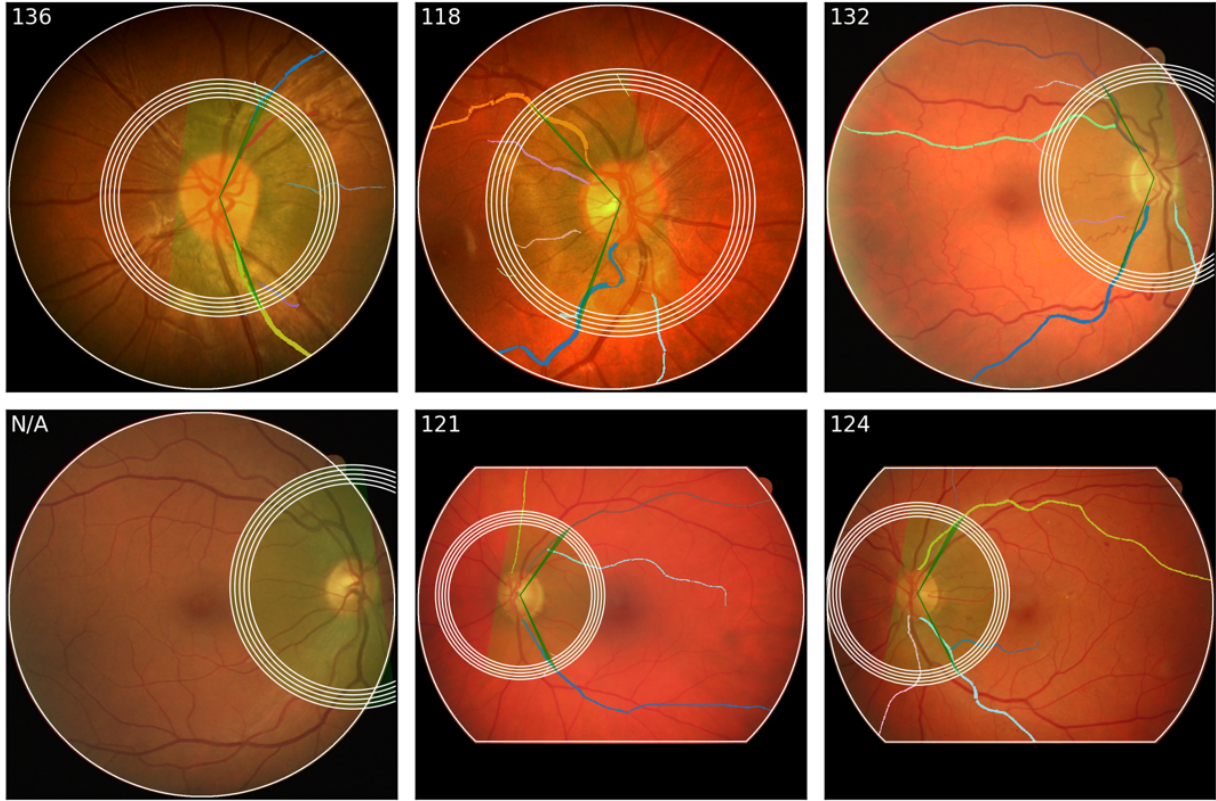


Figure 7. Examples of temporal angle computation capturing the opening angle of the main vascular arcades. The computed value is show on the top left corner of each sample.

**Sparsity.** Let  $DT(x)$  represent the distance transform over  $R$ , ie. the normalized Euclidean distance to the nearest vessel pixel (scaled by  $d_{ODF}$ ). Over pixels in  $R$  we report either the mean or the largest local maximum:

$$S_{\text{mean}} = \frac{1}{|R|} \sum_{x \in R} DT(x), \quad S_{\text{max}} = \max_{x \in R \cap \text{local maxima}} DT(x).$$

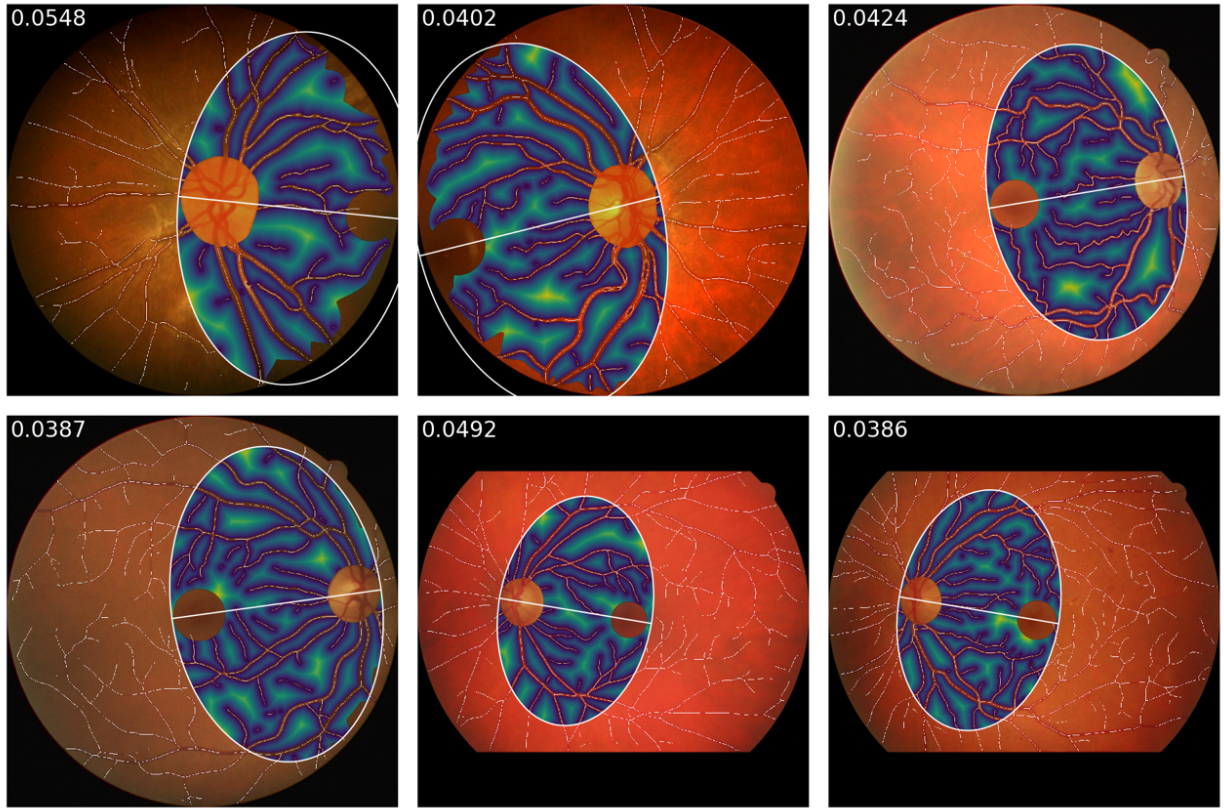


Figure 8. Examples of sparsity computation over a grid defined around the optic disc. The computed value is show on the top left corner of each sample.

**VarianceOfLaplacian.** For the fundus image  $I$  (grayscale), compute the discrete Laplacian  $L = \Delta I$ . Image sharpness is summarized as the variance over  $R$ :

$$\text{Var}\{L(x) : x \in R\}.$$

**DiscFoveaDistance.** With optic disc center  $c_{OD}$  and fovea position  $p_f$ ,

$$d_{ODF} = \|c_{OD} - p_f\|_2.$$

## Feature localisation

Most features in VascX can be configured with an optional `grid_field` parameter that specifies the region of interest. A grid can be understood as a subdivision of the image space (eg. the ETDRS grid), and a grid field as a particular region within that subdivision (eg. the outer ring of the ETDRS grid, the superior hemifield, or the entire grid). The optic disc mask and fovea position (e.g., OD–fovea axis) are usually used to orient geometry. Several grids are included with VascX (e.g., ETDRS grid, disc-centered grid, superior and inferior hemifields).

VascX models CFI bounds as a binary mask indicating the image region. By default, these are computed using the retinalysis-fundusprep package<sup>14</sup>, which fits a fundus circle and optional straight edges. For a given field, the platform first calculates the fraction of the field that is within the CFI bounds mask. Depending on the region imaged and the field of view of the CFI, it is possible that a large fraction of the field is out of bounds or not visible in the image. If the fraction within bounds is too small (< 0.5 by default), biomarker computation returns a null value to indicate an invalid measurement. If the field lies sufficiently within image bounds, biomarker computation will proceed using only the structures that lie within the field. Segments and full vessels are trimmed to the part of them that lies within the field. Nodes (endpoints, bifurcations) are included if their coordinates fall inside the field. Pixel/area-based measures (e.g., vascular density, tortuosity maps) are computed using the pixels inside the field mask only. Structures outside the chosen field are ignored for aggregation and summarization.

VascX includes the following predefined grids:

- **EllipseGrid**: ellipse centered midway between disc and fovea, major axis along OD–fovea. This grid has consistently high visibility in both optic disc and macula centered images. Fields: FullGrid, Superior, Inferior.
- **CircleGrid**: circle centered midway between disc and fovea (radius derived from OD–fovea distance and disc size). This grid provides consistent measurements on macula-centered images. Fields: FullGrid, Superior, Inferior.
- **ETDRSGrid**: classic macula-centered ETDRS layout with rings (Center, Inner, Outer), quadrants (Superior, Inferior, Nasal, Temporal, plus Left/Right), and subfields (CSF, SIM, NIM, TIM, IIM, SOM, NOM, TOM, IOM).
- **DiscCenteredGrid**: disc-anchored rings (inner, center, outer) and quadrants (superior, inferior, nasal, temporal, plus left/right), taking laterality into account. This grid is meant for consistent measurements on disc-centered images.
- **HemifieldGrid**: superior/inferior half-planes split relative to the OD–fovea axis. Fields: FullGrid, Superior, Inferior.

## Biomarker and grid scaling

While several vascx biomarkers such as tortuosity are unit-less, others such as vessel calibers or CREs measure distances. VascX, by default produces distance measurements in pixels and leaves the potential conversion of such measurements up to the user.

To support the most general use case where conversion factors are not available or are not trustworthy – common in real-world datasets, positioning and scaling of the different grids is done relative to anatomical landmarks – the optic-disc to fovea axis. Importantly, this includes the ETDRS grid. By default, VascX will position the ETDRS grid using an assumed distance of 4.75mm between the optic disc center and the fovea to derive a mm/pix scaling factor. This distance is a population-based measured in previous work <sup>15</sup>. In practice this means that the ETDRS grid in VascX is defined relative to optic-disc fovea distance rather than fixed distances from the optic disc.

If conversion factors are available, VascX supports an optional explicit `scaling_factor` argument, provided per sample. When provided, this factor will be used for both scaling of the ETDRS grid (overriding the 4.75mm OD-fovea distance assumption) and for conversion of output biomarkers into physical units.

## Biomarker arguments

In addition to arguments that enable feature localization (`grid_field`), VascX biomarkers have several optional arguments that affect computation. For example, the radius of the circles used for CRE computation, spline smoothing parameters used to compute tortuosity, or threshold used to define if a vessel segment belongs within a grid field, can be configured for a particular biomarker. While the platform includes sensible defaults calibrated to work on most standard CFIs, the ability for researchers to easily customize biomarkers is a core feature of the platform. Supplementary Table 1 shows a summary of current biomarker arguments and briefly describes their role.

## Evaluation

### Test-retest biomarker reproducibility

We provide validation of the biomarkers from `retinalysis-vascx` via test-retest reproducibility experiments. We made use of historical and recent imaging from the RS to compare the agreement between biomarkers extracted from images of the same eye taken by different cameras on the same patient visit. The temporal overlap in the imaging devices used in the RS allowed us to analyze 8 device pairs resulting from overlap in imaging from 7 Topcon devices used to image the cohort between 1990 and 2026. Although the images used were of the same eye, the field of view and image characteristics were often different between devices, and within device. Figure 9 shows sample images used in the evaluation for each device. We measured agreement via intra-class correlation coefficients (ICCs) using a Two-way Random Effects model – ICC(2,1), which assesses the absolute

agreement of single measurements, treating both eyes and devices as random effects. We stratified the images by field (F1 – OD-centered and F2 – fovea-centered) and applied quality control using our sparsity measures. Biomarkers measured in pixel units (calibers and CREs) were normalized by dividing by the optic-disc to fovea distance (also in pixels) to account for differences in scale. Figures 11 and 12 show the ICC for each (*biomarker, device*) pair along with the number of image pairs used in ICC computation. Note that a given pair was excluded from the score when one of the biomarkers was not computable on one of the two images (i.e. when *vascx* produced a *NULL* value).

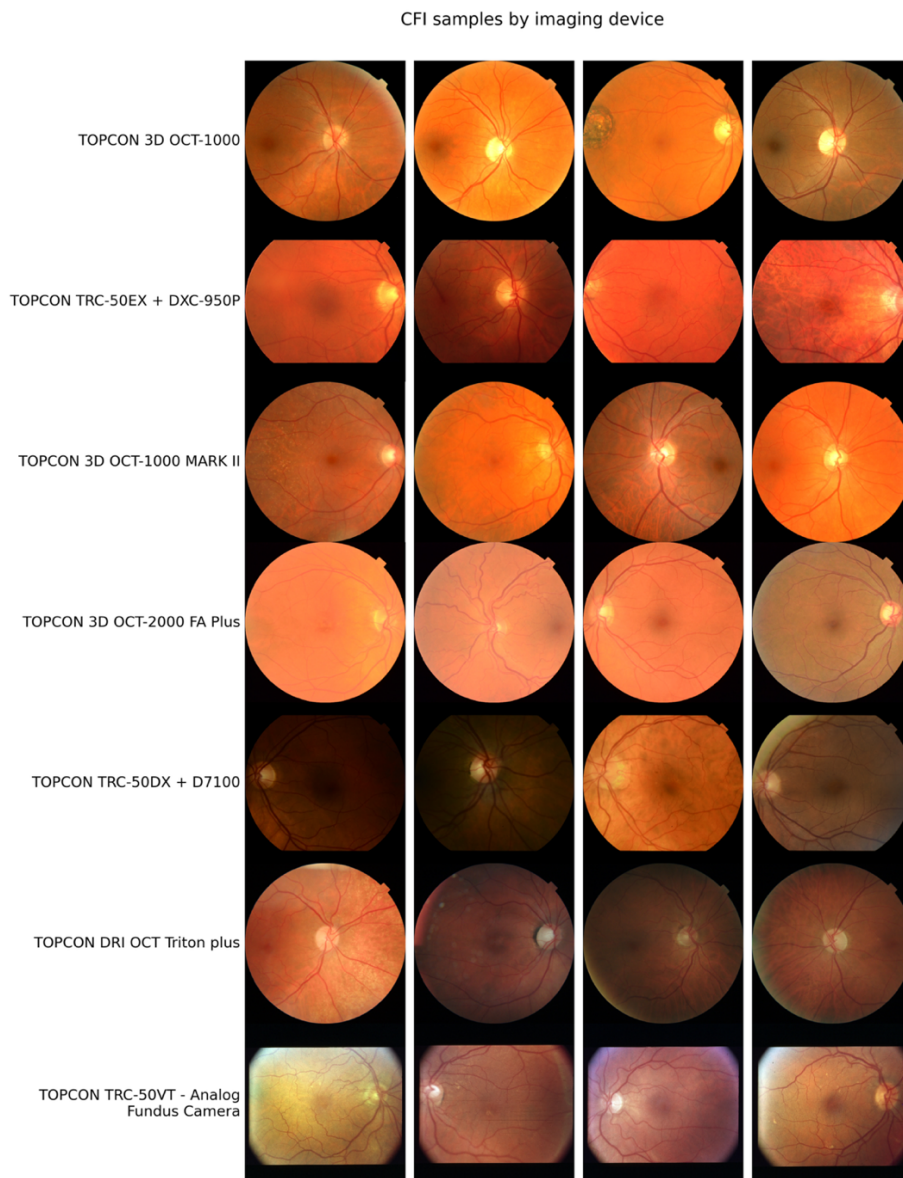


Figure 9. Sample images from the devices used in the cross-device test-retest biomarker reproducibility experiments.

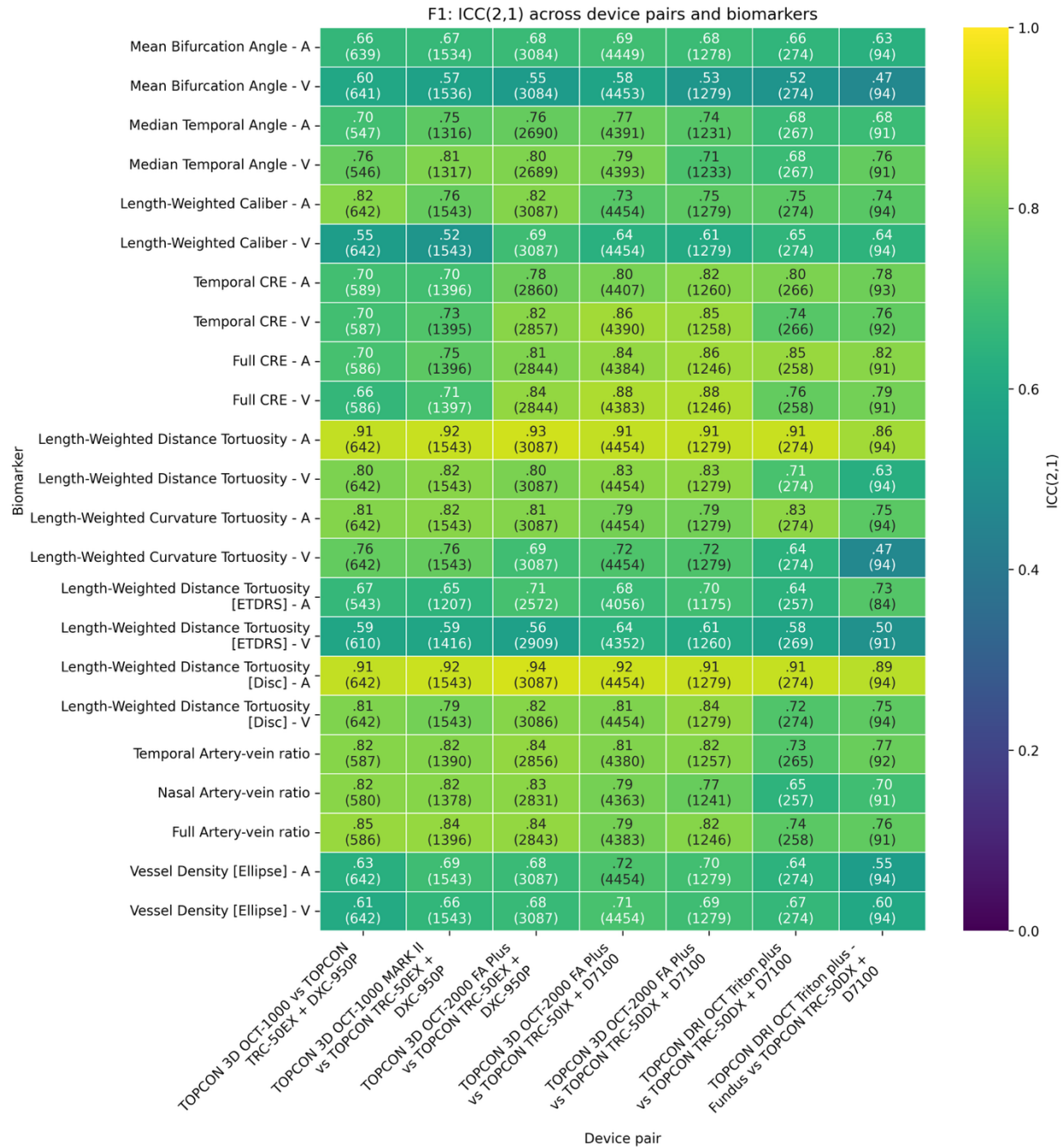


Figure 10. Biomarker test-retest agreement between measurements from images of the same eye by different CFI devices, for field-1 (F1) images (optic disc centered). Intra-class correlation coefficients were computed for each device pair (X axis) with overlapping imaging (on the same eyes) in the Rotterdam Study. Each cell displays the ICC(2,1) score (two-way random effects, absolute agreement, single measures) and in parentheses, the number of image pairs (N) used in the calculation of the score.

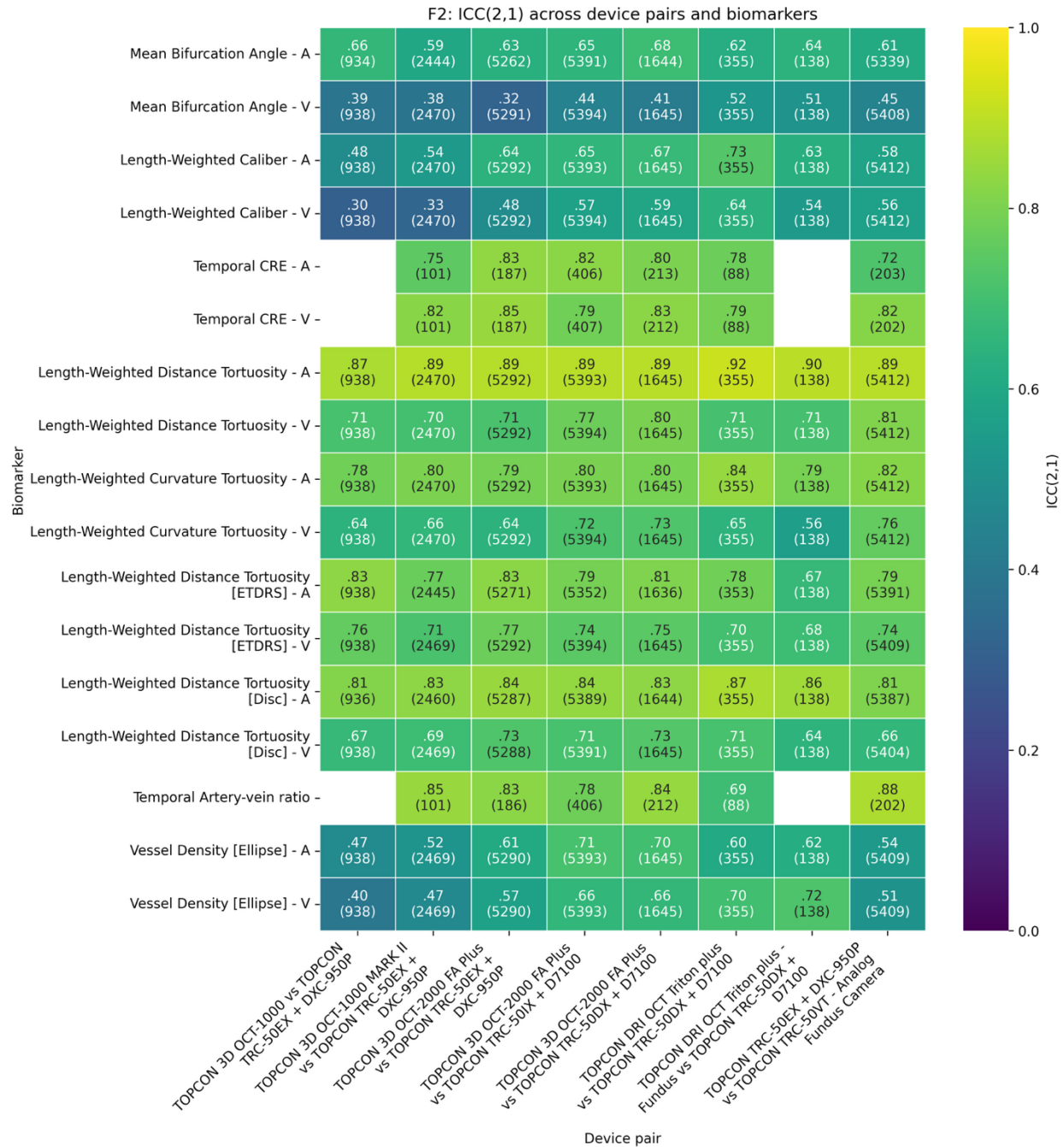


Figure 11. Biomarker test-retest agreement between measurements from images of the same eye by different CFI devices, for field-2 (F2) images (macula-centered). Intra-class correlation coefficients were computed for each device pair (X axis) with overlapping imaging (on the same eyes) in the Rotterdam Study. Each cell displays the ICC(2,1) score (two-way random effects, absolute agreement, single measures) and in parentheses, the number of image pairs (N) used in the calculation of the score. Blank cells had fewer than 50 valid biomarker pairs and were excluded from computation.

## Biomarker sensitivity analysis

Lower image quality levels are likely to degrade the quality of input segmentations used by retinalysis-vascx. In this analysis, we evaluate how different biomarkers perform across image quality levels. Because the degradation of segmentations due to low quality may be difficult to simulate, we instead perturbed source images with domain-relevant perturbations of different strengths before extracting biomarkers. We characterize the change in biomarker values (MAE and ICC(2,1) relative to the biomarker values on the original non-perturbed image with respect to the strength of the perturbation applied. In this way, we provide a measure of biomarker sensitivity to image degradation. A core feature of VascX is its ability to output a null value when the biomarker is not computable on a given image due to a lack of input data or because the computation regions are out of bounds. Next to MAE and ICC metrics, we characterize how the frequency of non-computable outputs changes with perturbation strength.

Our perturbation pipeline applies artifacts and other image transforms designed to mimic degradations present in real fundus images. The pipeline simulates, in order, diffuse artifacts (vitreous\_floaters, lens\_dust), uneven\_illumination (dark regions, vignetting), chromatic aberration, and blur (defocus blur, motion blur), and sensor noise. Appendix B shows a sample figure with augmented versions of four images.

Figures 12, 13, and 14 show the results of our biomarker sensitivity analysis for a representative set of biomarkers. We normalized MAE relative to the standard deviation of the original biomarker (non-perturbed) to obtain a measure that is comparable across biomarkers. ICCs were calculated following the same ICC(2,1) procedure used in the previous section.

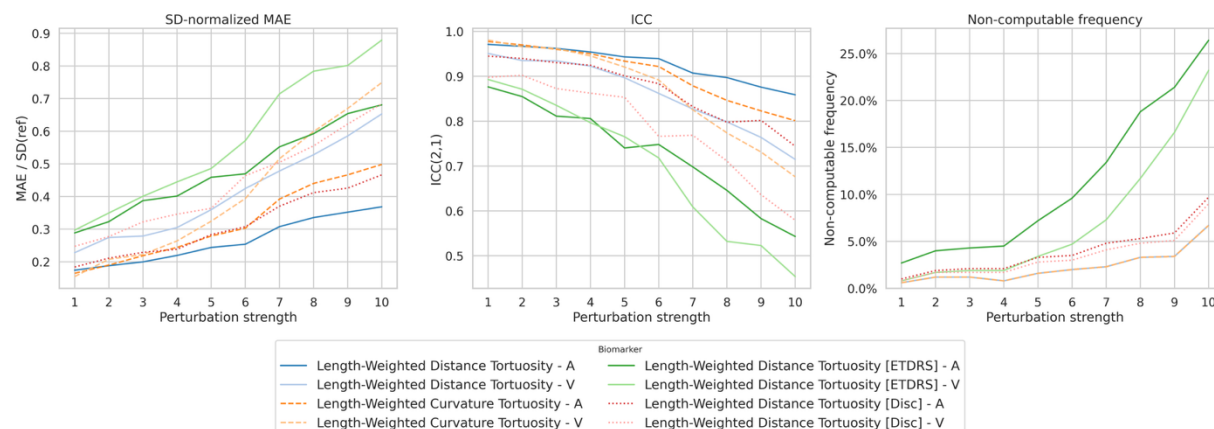


Figure 12. Results of our biomarker sensitivity analysis for tortuosity biomarkers. The plot shows normalized MAE and ICC relative to the non-perturbed biomarker values (Y axes)

against the strength of the perturbation applied to the image (X axis). The frequency of non-computable or null outputs per biomarker is shown on the right.

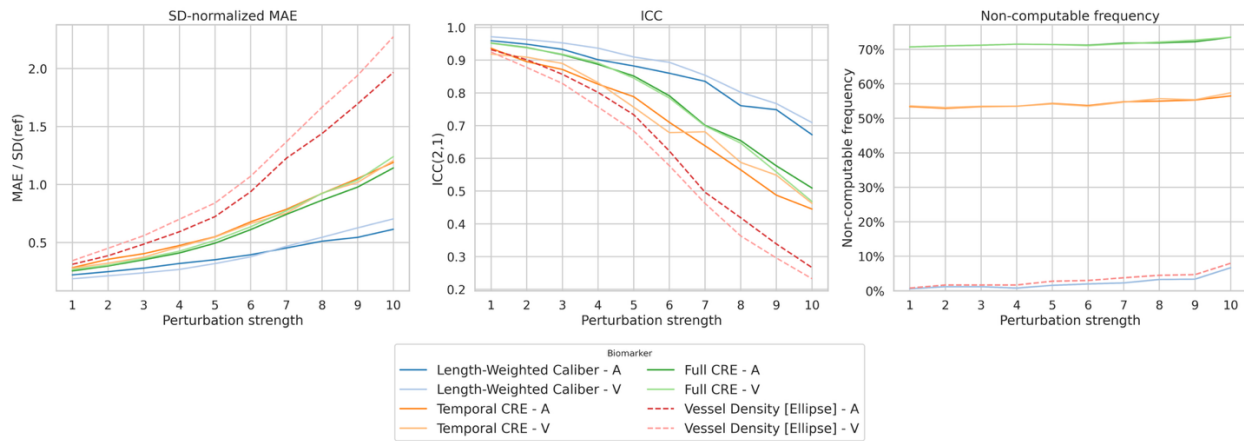


Figure 13. Results of our biomarker sensitivity analysis for caliber, CRE, and vascular density biomarkers. The plot shows normalized MAE and ICC relative to the non-perturbed biomarker values (Y axes) against the strength of the perturbation applied to the image (X axis). The frequency of non-computable or null outputs per biomarker is shown on the right.

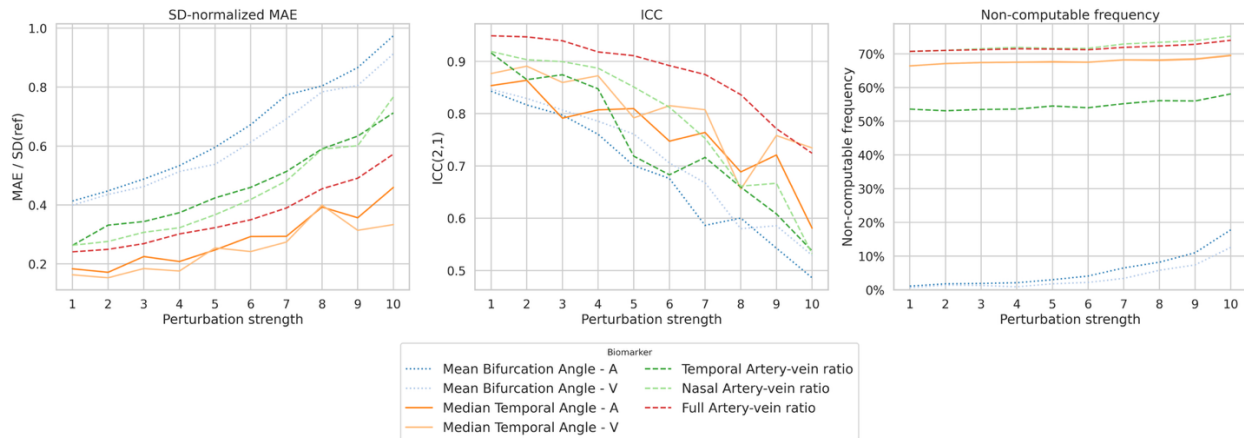


Figure 14. Results of our biomarker sensitivity analysis for bifurcation angle, temporal angles, and artery-vein ratio biomarkers. The plot shows normalized MAE and ICC relative to the non-perturbed biomarker values (Y axes) against the strength of the perturbation applied to the image (X axis). The frequency of non-computable or null outputs per biomarker is shown on the right.

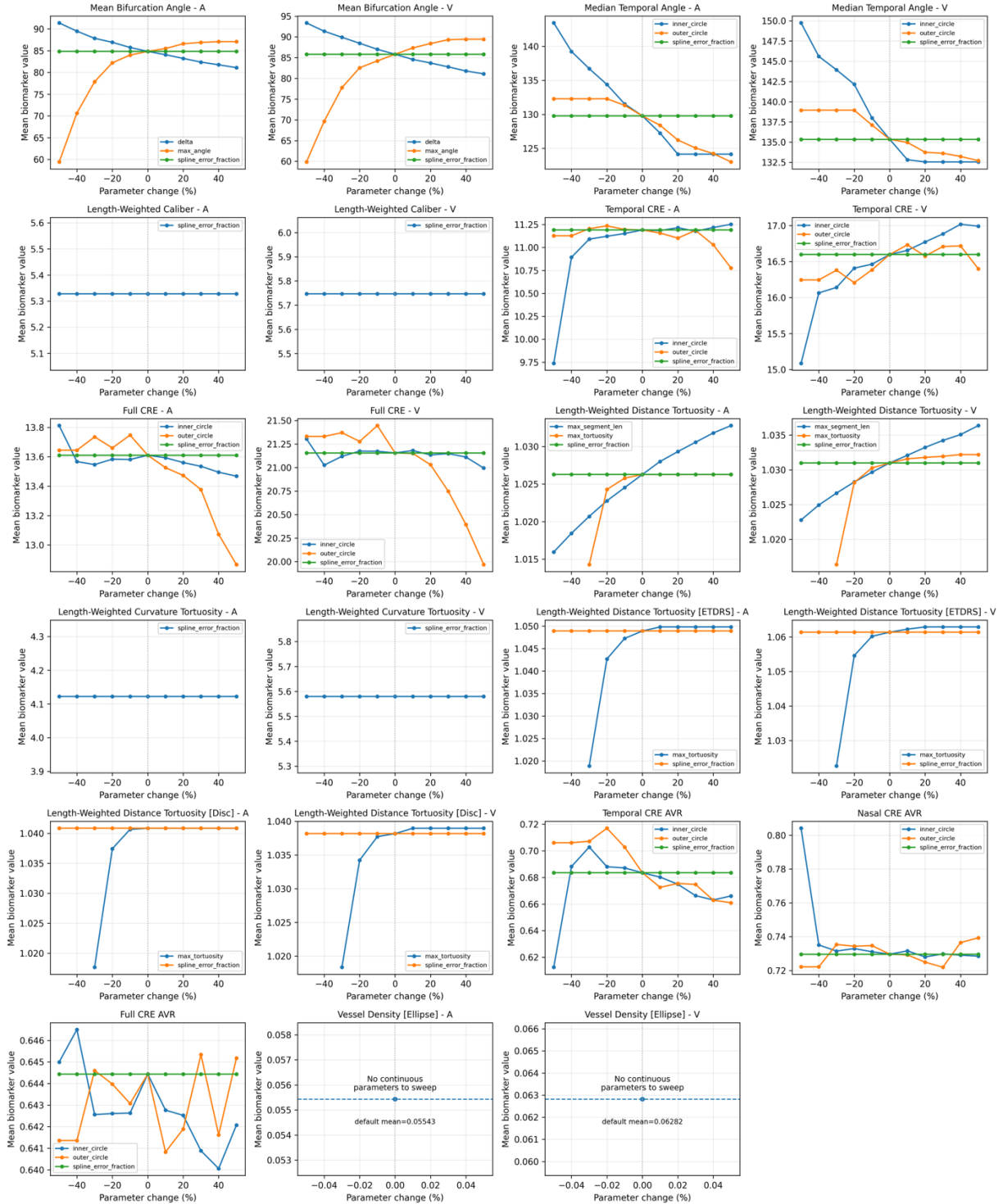


Figure 15. Parameter sensitivity analysis of VascX biomarkers. For each biomarker, the plot shows how changes in the value of continuous heuristic arguments affect the mean value of the biomarker. Plotted points are averages over a sample of 100 images.

In addition to image quality and device effects, each VascX biomarker has optional arguments that can be used to configure it (Appendix A). We complete our sensitivity analysis with experiments on the effect of biomarker arguments on VascX outputs.

We assessed how changes in vascx parameters affect its outputs on a subset of 100 randomly selected images (with QC as the only exclusion criterion) from the Rotterdam Study. For each of the representative biomarkers evaluated in the manuscript, one continuous parameter was changed at a time from its default value to study its effect in isolation while keeping the others constant. Biomarker values were changed in the range (-50%, +50%) relative to their default values. Figure 15 plots the results on the biomarker scale (Y axis).

## External usability

During its development, retinalysis-vascx has been used by the authors and external collaborators to run large-scale analysis of the vasculature on both large-scale population data and smaller disease-specific datasets<sup>16-19</sup>. Feedback from the author team and external users has been incorporated into the platform, both to refine the quality of the biomarkers and improve the ease of use of the software. A version of VascX has been adapted to the computation of OCTA vascular biomarkers<sup>20</sup>.

## Discussion

Our evaluation of retinalysis-vascx showed that the platform can extract reproducible biomarkers across a range of devices and image conditions. Our test-retest reproducibility analysis using extensive historical imaging from the Rotterdam Study to compare biomarkers on images of the same eye by different imaging devices revealed moderate to good agreement (ICC > 0.5) on most biomarkers and device pairs, with some showing excellent agreement (ICC > 0.9).

Bifurcation angles, vascular densities, and tortuosity measured in the ETDRS grid region were the least reproducible biomarkers, with some device pairs showing poor agreement. This can be explained by the fact that bifurcation angles are not robust against segmentation mistakes such as missing vessels or vessel mislabeling, which can cause a bifurcation to be missed entirely. Vascular density is likely affected by differences in the region imaged. Although we stratified images by field (macula-centered vs OD-centered), different devices had slightly different field of view and inconsistent centering. Tortuosity in the ETDRS region is likely affected by the lack of visibility of the small vessels in the macular region, which affects segmentation.

On the other hand, length-weighted tortuosity and CREs stood out as the most reproducible biomarkers. In the case of tortuosity, this could be explained by increased tortuosity manifesting across the entire retinal vasculature, making the biomarker particularly robust. CREs, on the other hand, are driven by the caliber measurements of a few, but usually thick vessels close to the optic disc. The thickness of these vessels makes them unlikely to be lost to measurement due to image quality degradation.

Bifurcation angles, calibers, and tortuosity show reduced reproducibility for veins when compared to arteries. This stands out given that vein segmentation is known to have a higher Dice score performance in artery-vein segmentation when compared to arteries<sup>10</sup> and veins, which exhibit higher contrast with the CFI background. In the case of tortuosity, this can be explained by the fact that tortuosity is not invariant to the splitting of a vessel segment (ie. a half circle split in two has lower tortuosity than a connected half circle). For other biomarkers, this trend may be driven by inconsistent visibility of the smallest veins. Small arteries may be consistently under-segmented due to their lower contrast, while small veins are inconsistently segmented, resulting in less consistent vein biomarkers.

Our biomarker sensitivity analysis, designed to test robustness against perturbations of the CFIs, showed generally consistent results on both normalized MAE and ICC metrics. As expected, biomarkers exhibited a steady decline with perturbation strength. The lower robustness of bifurcation angles, vessel densities, and ETDRS-localized biomarkers was consistent with the findings of the reproducibility analysis. Tortuosity measurements were, in general, more robust than caliber measurements. Vessel densities were remarkably affected, likely due to the perturbations causing under-segmentation. Global tortuosity, calibers, CRE, and artery-vein ratios were more robust to perturbation.

Interestingly, CREs were less robust to perturbation than length-weighted caliber measurements, contrary to the cross-device reproducibility results in which CREs were slightly more reproducible. This suggests the presence of a different mechanism driving the device differences that is not modeled in the perturbation pipeline. Differences in imaged region or CFI field of view, for example, may be a primary factor driving cross-device differences in length-weighted calibers, as regions away from the optic disc have thinner vessels. This factor source of error is not present in the image perturbation experiments.

The frequency of null or non-computable outputs (Figures 12-14) showed the expected behavior, with a mild increase from baseline frequencies for most biomarkers. Baseline null frequencies were the highest (~70%) for CREs and temporal angles. This is expected as CREs can only be computed on OD-centered images, which were about 30% of our evaluation set. Temporal Angles similarly require a large region close to the optic disc to be

visible in the image, and the OD was too close to the image bounds in many of our macula-centered images. Artery-vein ratios had similar rates due to being derived from CREs. The rest of the biomarkers were computable on most images at baseline, but the frequency of null outputs increased sharply with perturbation strength. The ETDRS / macular region tortuosity biomarkers were the most affected because noise and blur perturbations affect the segmentation of small vessels the most. It must be noted that VascX's ability to output null values in certain non-computable scenarios is not a substitute for a quality control step, which is not part of biomarker computation.

Finally, our parameter sensitivity analysis (Figure 15) showed that most vascx biomarkers exhibit, in most cases, little systematic bias with respect to their optional arguments. The spline smoothing parameter, which controls the smoothness of the splines used to model vessel centerlines, for example, has negligible influence on computation. Some parameters defining computation regions and thresholds, such as inner and outer circles used for Temporal Angle and CRE computation, or the threshold used to filter out invalid tortuosity measurements, however, have a larger effect on the outputs, as expected.

## Potential uses for the software

The VascX pipeline has a variety of potential use cases:

- **Oculomics and cardiovascular risk modeling:** Generate standardized, OD–fovea-aligned and ETDRS-grid biomarkers (morphology, topology, caliber) from artery–vein–resolved segmentations to support association studies and risk prediction for systemic outcomes.
- **Clinical and epidemiological research:** Report region-aware measurements (e.g., CRE, temporal arcade angle, tortuosity) in harmonized subfields, enabling reproducible, cross-center analyses and longitudinal studies, including reproducibility across repeat images of the same eye.
- **Population-scale pipelines and biobanks:** Run high-throughput batch extraction from pre-segmented images to produce analysis-ready feature tables suitable for large cohorts and multi-center datasets.
- **Biomarker development and benchmarking:** Use the modular, graph-based pipeline (skeleton → undirected graph → directed tree → resolved vessels) to prototype and compare new biomarkers or aggregation strategies with clear intermediate representations.
- **Adaptation to other modalities or use cases:** The VascX pipeline is highly modular and its building blocks may be adapted to different modalities or extended with new functionality.

## Limitations of the software

VascX relies on external segmentations (vessels, artery/vein, optic disc, fovea), and their accuracy directly conditions all derived biomarkers. Errors such as missed or spurious vessels, artery–vein misclassification, or mislocalized disc/fovea—often caused by fundus image quality issues (e.g., blur, artifacts, illumination, limited field-of-view)—can bias both global and region-aware (ETDRS, OD–fovea–aligned) measurements. Users should treat segmentation quality and image quality as potential confounders and assess whether these preconditions are adequate for their study; sensitivity analyses and additional QC may be warranted before deciding to use the software in each setting. The authors encourage and welcome follow-up work to quantify and mitigate the effects of image quality and segmentation errors on retinal vascular biomarkers.

A second limitation of the pipeline is that it is currently designed specifically for enface images, usually containing either the fovea or optic disc. However, its modular design and clear structure enable its adaptation to other use cases.

## Acknowledgments

The authors acknowledge the staff of the Eyed Reading Center for their different roles in the project. Special acknowledgement to the Sinergia consortium for conceiving and supporting this project; and for their valuable feedback on the VascX platform. This work was funded by the Swiss National Science Foundation grant no. CRSII5 209510. Generative AI was used in the preparation of this manuscript as assistance in writing and proofreading. Google Gemini 2 and 3 were used in the period between July 1, 2025 and January 26, 2026.

## References

1. Patterson EJ, Bounds AD, Wagner SK, Kadri-Langford R, Taylor R, Daly D. Oculomics: A Crusade Against the Four Horsemen of Chronic Disease. *Ophthalmol Ther*. 2024;13(6):1427-1451. doi:10.1007/s40123-024-00942-x
2. Zhu Z, Wang Y, Qi Z, et al. Oculomics: Current concepts and evidence. *Prog Retin Eye Res*. 2025;106:101350. doi:10.1016/j.preteyeres.2025.101350
3. Wagner SK, Fu DJ, Faes L, et al. Insights into Systemic Disease through Retinal Imaging-Based Oculomics. *Transl Vis Sci Technol*. 2020;9(2):6. doi:10.1167/tvst.9.2.6
4. Ortín Vela S, Beyeler MJ, Trofimova O, et al. Phenotypic and Genetic Characteristics of Retinal Vascular Parameters and their Association with Diseases. *medRxiv*. Published online 2023. doi:10.1101/2023.07.07.23292368
5. Abdulsahib AA, Mahmoud MA, Aris H, Gunasekaran SS, Mohammed MA. An Automated Image Segmentation and Useful Feature Extraction Algorithm for Retinal Blood Vessels in Fundus Images. *Electronics*. 2022;11(9). doi:10.3390/electronics11091295
6. Retinal vascular geometry detection as a biomarker in diabetes mellitus. doi:10.1177/11206721211033488
7. Galdran A, Anjos A, Dolz J, Chakor H, Lombaert H, Ayed IB. The Little W-Net That Could: State-of-the-Art Retinal Vessel Segmentation with Minimalistic Models. Published online 2020.
8. Fhima J, Van Eijgen J, Billen Moulin-Romsée MI, others. LUNet: deep learning for the segmentation of arterioles and venules in high resolution fundus images. *Physiological Measurement*. 2024;45(5):10.1088/1361-6579/ad3d28. doi:10.1088/1361-6579/ad3d28
9. Zhou Y, Wagner SK, Chia MA, et al. AutoMorph: Automated Retinal Vascular Morphology Quantification Via a Deep Learning Pipeline. *Translational Vision Science & Technology*. 2022;11(7):12. doi:10.1167/tvst.11.7.12
10. Vargas Quiros J, Liefers B, van Garderen KA, Vermeulen JP, Klaver C. VascX Models: Deep Ensembles for Retinal Vascular Analysis From Color Fundus Images. *Trans Vis Sci Tech*. 2025;14(7):19. doi:10.1167/tvst.14.7.19
11. Quiros JV, Liefers B, Garderen K van, Vermeulen J, Center ER, Klaver C. Rotterdam artery-vein segmentation (RAV) dataset. *arXiv*. Preprint posted online February 18, 2026:arXiv:2512.17322. doi:10.48550/arXiv.2512.17322
12. Fhima J, Eijgen JV, Stalmans I, Men Y, Freiman M, Behar JA. PVBM: A Python Vasculature Biomarker Toolbox Based on Retinal Blood Vessel Segmentation. In:

Karlinsky L, Michaeli T, Nishino K, eds. *Computer Vision – ECCV 2022 Workshops*. Springer Nature Switzerland; 2023:296-312. doi:10.1007/978-3-031-25066-8\_15

13. Knudtson MD, Lee KE, Hubbard LD, Wong TY, Klein R, Klein BEK. Revised formulas for summarizing retinal vessel diameters. *Current Eye Research*. 2003;27(3):143-149. doi:10.1076/ceyr.27.3.143.16049
14. Quiros JV, Liefers B, Garderen K van, Center ER, Klaver C. retinalysis-fundusprep: A python package for robust color fundus image bounds extraction. *arXiv*. Preprint posted online December 17, 2025:arXiv:2512.16044. doi:10.48550/arXiv.2512.16044
15. Jonas RA, Wang YX, Yang H, et al. Optic Disc-Fovea Distance, Axial Length and Parapapillary Zones. The Beijing Eye Study 2011. *PLoS One*. 2015;10(9):e0138701. doi:10.1371/journal.pone.0138701
16. Trofimova O, Böttger L, Bors S, et al. Deep learning aging marker from retinal images unveils sex-specific clinical and genetic signatures. *medRxiv*. Preprint posted online October 5, 2025:2025.07.29.25332359. doi:10.1101/2025.07.29.25332359
17. Beyeler MJ, Trofimova O, Bontempi D, et al. Comparing tangible retinal image characteristics with deep learning features reveals their complementarity for gene association and disease prediction. *medRxiv*. Preprint posted online January 13, 2026:2024.12.23.24319548. doi:10.1101/2024.12.23.24319548
18. Quintas I, Bontempi D, Bors S, et al. RetFit: A Novel Deep Learning-Based Biomarker of Cardiorespiratory Fitness Derived From the Retina. *medRxiv*. Preprint posted online January 26, 2026:2025.09.29.25336874. doi:10.1101/2025.09.29.25336874
19. Putera I, Quiros JDV, Rombach SM, Dik WA, van Hagen PM, La Distia Nora R. Artificial Intelligence-Based Uveitis Diagnosis Through Retinal Vasculature Analysis: A Paradigm Shift in Ocular Tuberculosis. *Ophthalmol Ther*. 2025;14(4):717-732. doi:10.1007/s40123-025-01103-4
20. Elwakil A, Martin T, Quiros JV, et al. CapillaryX: A Fine-Tunable Pipeline for OCTA Segmentation and Feature Extraction. *Research Square*. Preprint posted online November 25, 2025. doi:10.21203/rs.3.rs-8176394/v1

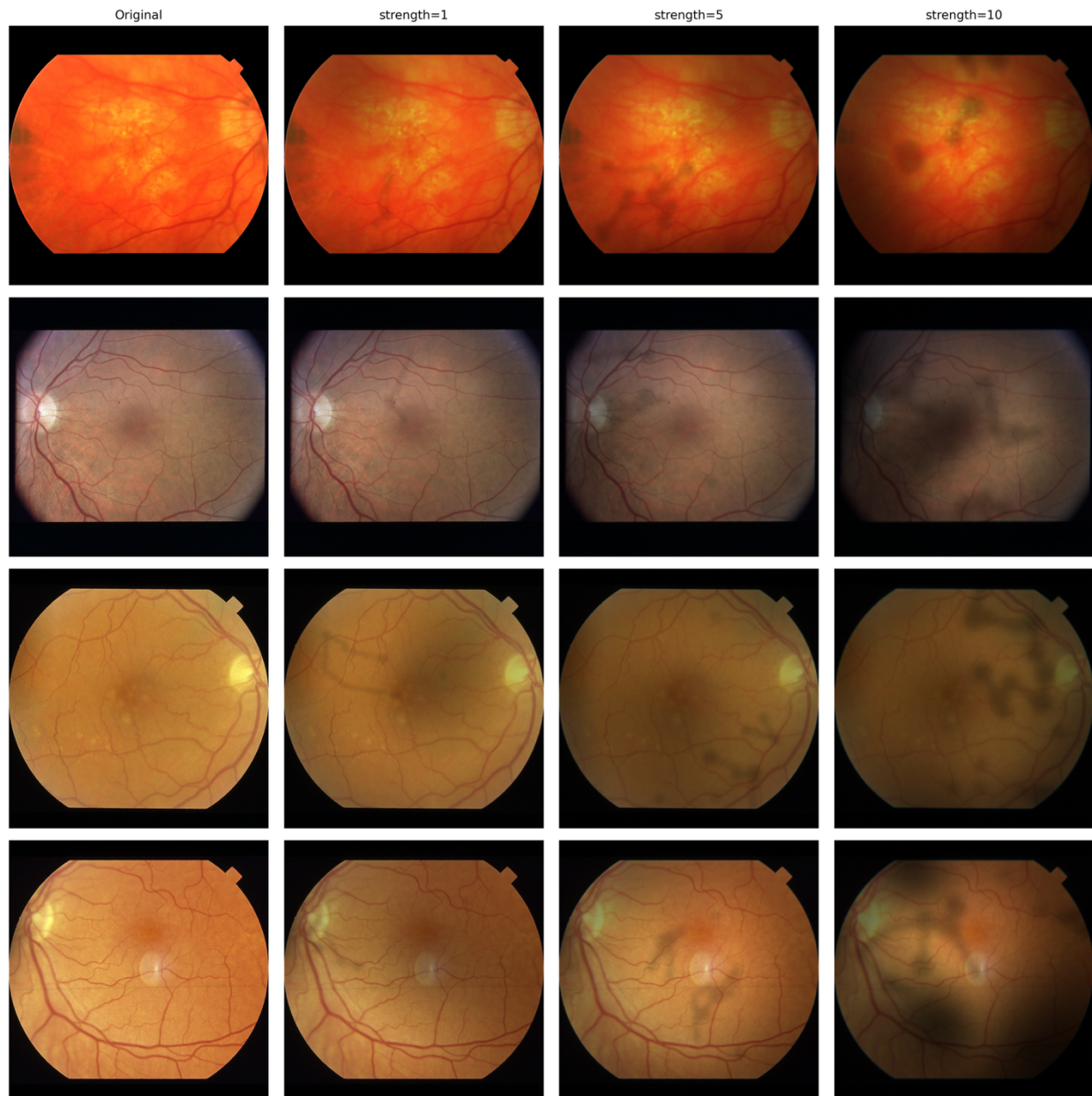
## Appendix A. Optional biomarker arguments

Table 1. VascX biomarker optional arguments and description of their role in computation.

Biomarker Name	Optional Arguments
<b>BifurcationAngles</b>	<ul style="list-style-type: none"> <li>- <b>delta</b> (20): Distance in pixels from the bifurcation where outgoing branch directions are sampled.</li> <li>- <b>max_angle</b> (135): Maximum bifurcation angle, in degrees, kept before aggregation.</li> <li>- <b>min_bifurcations</b> (3): Minimum number of valid bifurcations required to return a value.</li> <li>- <b>spline_error_fraction</b> (0.05): Spline fitting tolerance used when estimating branch directions.</li> <li>- <b>aggregator</b> (<i>mean</i>): Callable used to combine per-bifurcation angles.</li> </ul>
<b>BifurcationCount</b>	<ul style="list-style-type: none"> <li>- No constructor arguments besides <i>grid_field</i>.</li> </ul>
<b>Caliber</b>	<ul style="list-style-type: none"> <li>- <b>min_numpoints</b> (10): Minimum number of skeleton points a segment must have to be included.</li> <li>- <b>aggregator</b> (<i>median</i>): Callable used to combine per-segment median diameters. Can also be <i>LengthWeightedAggregator</i>.</li> <li>- <b>spline_error_fraction</b> (0.05): Spline fitting tolerance used for diameter estimation and length weighting.</li> </ul>
<b>CRE</b>	<ul style="list-style-type: none"> <li>- <b>CREMode</b> (<i>CREMode.Temporal</i>): Vessel-selection mode around the disc. Options are <i>Temporal</i>, <i>Nasal</i>, or <i>Full</i>.</li> <li>- <b>max_vessels</b> (6): Maximum number of largest intersecting vessels kept at each circle.</li> <li>- <b>hemifield</b> (<i>None</i>): Optional superior or inferior hemifield restriction.</li> <li>- <b>min_circles</b> (6): Minimum number of valid circles required to return a value.</li> <li>- <b>inner_circle</b> (1.0): Inner sampling radius in optic-disc-diameter multiples.</li> <li>- <b>outer_circle</b> (1.5): Outer sampling radius in optic-disc-diameter multiples.</li> <li>- <b>num_circles</b> (6): Number of concentric circles sampled between the inner and outer radii.</li> <li>- <b>spline_error_fraction</b> (0.05): Spline fitting tolerance used for circle intersections and caliber estimation.</li> </ul>
<b>Sparsity</b>	<ul style="list-style-type: none"> <li>- <b>mode</b> (<i>SparsityMode.MEAN</i>): Sparsity summary mode. Options are <i>MEAN</i> and <i>MAX</i>.</li> <li>- <b>normalize</b> (<i>True</i>): Whether to divide distances by the disc-fovea distance.</li> </ul>

<b>TemporalAngle</b>	<ul style="list-style-type: none"> <li>- <b>inner_circle</b> (2 / 3): Inner sampling radius as a fraction of the disc-fovea distance.</li> <li>- <b>outer_circle</b> (2 / 3 + 4 * 0.03): Outer sampling radius as a fraction of the disc-fovea distance.</li> <li>- <b>num_circles</b> (5): Number of concentric circles sampled between the inner and outer radii.</li> <li>- <b>spline_error_fraction</b> (0.05): Spline fitting tolerance used for circle intersections and pair geometry.</li> </ul>
<b>Tortuosity</b>	<ul style="list-style-type: none"> <li>- <b>mode</b> (<i>TortuosityMode.Segments</i>): Whether tortuosity is computed on segments or resolved vessels.</li> <li>- <b>measure</b> (<i>TortuosityMeasure.Distance</i>): Tortuosity definition. Options are <i>Distance</i>, <i>Curvature</i>, and <i>Inflections</i>.</li> <li>- <b>length_measure</b> (<i>LengthMeasure.Splines</i>): Length source used for distance tortuosity.</li> <li>- <b>min_numpoints</b> (25): Minimum number of skeleton points required for inclusion.</li> <li>- <b>max_segment_len</b> (<i>None</i>): Optional maximum split length, as a fraction of disc-fovea distance, used only for segment-mode distance tortuosity.</li> <li>- <b>max_tortuosity</b> (<i>None</i>): Optional upper cutoff for distance tortuosity. If left as <i>None</i>, the class uses 1.5 for distance tortuosity and no cutoff otherwise.</li> <li>- <b>aggregator</b> (<i>median</i>): Callable used to combine per-segment or per-vessel tortuosity values. Can also be <i>LengthWeightedAggregator</i>.</li> <li>- <b>spline_error_fraction</b> (<i>None</i>): Spline fitting tolerance used before tortuosity computation. If left as <i>None</i>, the class uses 0.05 for distance tortuosity and 0.25 for curvature or inflection tortuosity.</li> </ul>
<b>VascularDensity</b>	<ul style="list-style-type: none"> <li>- No constructor arguments besides <i>grid_field</i>.</li> </ul>

## Appendix B. Biomarker sensitivity analysis



*Figure 16. Sample images from our CFI augmentation pipeline used in the biomarker sensitivity analysis. The left-most column shows the four original samples. Each row displays an image with perturbations of different strengths applied to it.*

## Appendix C

The VascX Research Consortium (in alphabetical order):

Ciara Bergin 3; Sven Bergmann 1,2,4; Michael Beyeler 1,2,5; Dennis Bontempi 1,2; Sacha Bors 1,2; Leah Böttger 1,2; Bogdan Draganski 5,6,7; Adham Elwakil 3,8; Györgyi V. Hamvas 9,10; Janna Hastings 11,12; Ilaria Iuliani 1,2; Caroline C.W. Klaver 13,14,15,16; Ihor Kuras 6,7; Bart Liefers 13,14; Ilenia Meloni 3,8; Sofia Ortin Vela 1,2; David Presby 1,2; Ian Quintas 1,2; José Vargas Quiros 13,14,; Marc Schindewolf 9,10; Reinier O. Schlingemann 3,17; Mattia Tomasoni 3,8; Olga Trofimova 1,2.

1 Department of Computational Biology, University of Lausanne, Lausanne, Switzerland

2 Swiss Institute of Bioinformatics, Lausanne, Switzerland

3 Department of Ophthalmology, University of Lausanne, Fondation Asile des Aveugles, Jules Gonin Eye Hospital, Lausanne, Switzerland.

4 Department of Integrative Biomedical Sciences, University of Cape Town, Cape Town, South Africa

5 Insel University Hospital Bern, Switzerland

6 Department of Neurology, Max Planck Institute for Human Cognitive and Brain Sciences, Germany

7 Department of Clinical Neuroscience, Lausanne University Hospital and University of Lausanne, Switzerland

8 Platform for Research in Ocular Imaging, Fondation Asile des Aveugles, Jules Gonin Eye Hospital, Lausanne, Switzerland.

9 Inselspital, Bern University Hospital, University of Bern, Switzerland.

10 Department for BioMedical Research, Bern University Hospital, University of Bern, Switzerland.

11 Institute for Implementation Science in Health Care, Faculty of Medicine, University of Zurich, Zürich, Switzerland

12 School of Medicine, University of St Gallen, St. Gallen, Switzerland

13 Department of Ophthalmology, Erasmus University Medical Center, Rotterdam, The Netherlands.

14 Department of Epidemiology, Erasmus University Medical Center, Rotterdam, The Netherlands.

15 Department of Ophthalmology, Radboud University Medical Center, Nijmegen, the Netherlands.

16 Institute of Molecular and Clinical Ophthalmology, University of Basel, Switzerland.

17 University Medical Centres, Amsterdam, The Netherlands.